

11-14-2011

Electronic Structure of Realistically Extended Atomistically Resolved Disordered Si:P δ -doped Layers

Sunhee Lee

Purdue University - Main Campus

Hoon Ryu

Korea Inst. of Sci. and Technology Information

Llyd C. L. Hollenberg

University of Melbourne, Australia

Michelle Y. Simmons

University of New South Wales

Gerhard Klimeck

Purdue University - Main Campus, gekco@purdue.edu

Follow this and additional works at: <http://docs.lib.purdue.edu/nanopub>



Part of the [Nanoscience and Nanotechnology Commons](#)

Lee, Sunhee; Ryu, Hoon; Hollenberg, Llyd C. L.; Simmons, Michelle Y.; and Klimeck, Gerhard, "Electronic Structure of Realistically Extended Atomistically Resolved Disordered Si:P δ -doped Layers" (2011). *Birck and NCN Publications*. Paper 789.

<http://docs.lib.purdue.edu/nanopub/789>

Electronic structure of realistically extended atomistically resolved disordered Si:P δ -doped layersSunhee Lee,^{1,*} Hoon Ryu,^{1,2,†} Huw Campbell,^{3,‡} Lloyd C. L. Hollenberg,⁴ Michelle Y. Simmons,³ and Gerhard Klimeck¹¹*Network for Computational Nanotechnology (NCN), Birck Nanotechnology Center, Purdue University, West Lafayette, Indiana 47906, USA*²*Supercomputing Center, Korea Institute of Science and Technology Information (KISTI)
52-11 Eoeun-dong, Yuseong-gu, Daejeon 305-806, Republic of Korea*³*Centre for Quantum Computation and Communication Technology, School of Physics,
University of New South Wales, Sydney, New South Wales 2052, Australia*⁴*Centre for Quantum Computation and Communication Technology, School of Physics,
University of Melbourne, Melbourne, Victoria 3010, Australia*

(Received 3 August 2011; revised manuscript received 12 October 2011; published 14 November 2011)

The emergence of scanning tunneling microscope (STM) lithography and low temperature molecular beam epitaxy (MBE) opens the possibility of creating scalable donor based quantum computing architectures. In particular, atomically precise Si:P monolayer structures (δ -doped layers) serve as crucial contact regions and in-plane gates in single impurity devices. In this paper we study highly confined δ -doped layers to explain the disorder in the P dopant placements in realistically extended systems. The band structure is computed using the tight-binding formalism and charge-potential self-consistency. The exchange-correlation corrected impurity potential pulls down subbands below the silicon valley minima to create impurity bands. Our methodology is benchmarked and validated against other theoretical methods for small ordered systems. The doping density is shown to linearly control the impurity bands. Disorder within the Si:P δ -doped layer is examined using an extended domain to describe the effects of experimentally unavoidable randomness through explicitly disordered dopant placement. Disorder in the δ -doped layer breaks the symmetry in the supercell and creates band splitting in every subband. Vertical segregation of dopants is shown to dramatically reduce valley splitting (VS). Such VS can be used as a measure of ideality of the fabricated Si:P δ -doped layer. Although the resulting disorder induces density of states fluctuations, this theoretical analysis shows that δ -doped layers can serve as quasimetallic 2D electron sources even in the presence of strong nonidealities.

DOI: [10.1103/PhysRevB.84.205309](https://doi.org/10.1103/PhysRevB.84.205309)

PACS number(s): 71.15.-m, 71.23.-k, 73.22.-f

I. INTRODUCTION

There has been rapid progress using scanning tunneling microscopy (STM) to pattern phosphorus donors in silicon using phosphine gas and then encapsulating them with low temperature molecular beam epitaxy (MBE).^{1,2} The combination of these two technologies has created the possibility for controlling dopant placement in silicon with atomic-scale precision in all three dimensions. Using this technology, experimentalists have built a variety of planar, highly doped phosphorus δ -doped devices embedded in silicon (Si:P) such as tunnel junctions, quantum dots, and nanowires.³⁻⁵ More importantly, the precise incorporation of donors enables the potential realization of donor-based quantum computers.⁶⁻¹⁰

Central to these planar Si:P device architectures is a highly conductive 2D δ -doped sheet.¹¹⁻¹⁴ By patterning the 2D δ -doped layers into specific geometries, they can act as both Ohmic contacts as well as gates for the control of electron and spin transport through singly placed donor impurities in quantum computing architectures. Understanding the impact of impurity placement and position both within the plane and vertically in 2D δ -doped sheets is important for understanding the electron transport in highly confined, STM-patterned architectures and essential for continuing efforts in experimental device design.

Over the past few years a detailed understanding of the incorporation mechanism of P atoms into silicon using phosphine gas has been developed.¹⁵⁻¹⁷ From this understanding it has been possible to use an STM to lithographically position single P atoms into the top atomic layer of silicon by opening

a hole in a hydrogen resist and annealing to temperatures of 350 °C.¹⁷ This anneal causes the phosphine gas to lose its hydrogen atoms on the surface before a single P atom can incorporate into the top layer of silicon, displacing a silicon atom. The incorporation anneal can also be performed on a phosphine saturation dosed sample. At saturation dosing after room-temperature exposure, depending on the dosing conditions the surface coverage will be a disordered alloy of PH₂ + H and PH + 2H. However, after the incorporation anneal the final P dopant density invariably takes the nominal value of 0.20–0.25 ML with the P atoms located in random positions within the top layer of the Si surface.¹⁶ The high doping density means that the P atoms are typically 1 nm apart, which is much smaller than the Bohr radius. As a result, one can expect extensive wave function overlap and metallic-like behavior within atomically controlled 2D nanostructured domains.

There have been efforts made to experimentally identify the electronic structure of MBE fabricated δ -doped layer in silicon by Eisele *et al.* using resonant tunneling spectroscopy.¹⁸⁻²⁰ The fabricated δ -doped layer was about 2 nm thick with the doping density exceeding 10^{13} cm⁻² and it showed quantized energy levels originating from 2D subbands confined in the layer. To compute the electronic structure of δ -doped layers, several theoretical studies have been published. Initially, the potential profile was computed using a Thomas-Fermi approximation and then subsequently superimposed to the diagonal elements of the Schrödinger equation to compute confined energy levels in different types of δ layers in silicon.²¹⁻²⁴ More rigorous

self-consistent calculations were carried out by Qian *et al.* by computing such systems using planar Wannier orbitals based on an empirical pseudopotential method (PP) and parabolic dispersions of silicon subbands.²⁵ Cartoixà *et al.* focused on determining Fermi level fluctuations with temperature and doping density in the Si:P δ -layer structure using atomistic sp^3s^* tight-binding (TB) calculations with an antibonding orbital model.²⁶ However the sp^3s^* model is well known to misrepresent X points in the conduction band,²⁷ and it is clear that the basis size is too small to describe L and X valleys.^{27–29} Carter *et al.* has calculated band structures of Si:P δ -doped layers using different atom configurations within density functional theory (DFT).³⁰ The computational burden of DFT calculations, however, prevents the method from extending to 2D systems and structures with realistic degrees of disorder, which require large supercell domains. To overcome the computational limitation, a mixed-atom pseudopotential (MP) was recently examined, which reduces the level of *ab initio* input. This method has been shown to compare well with earlier theoretical studies.³¹ In the MP approach, however, atomistic effects cannot be handled since the model assumes an averaged nuclear charge between silicon and phosphorus in the δ layer.

Thus, to date all theoretical works have focused on either ordered configurations or limited disorder using small domain sizes; none of them have been able to investigate the effect of realistic disorder in Si:P δ -doped layers using an *extended* domain, which is critical for a reasonable approximation of random dopant placement. Examining how disorder plays a role in the electronic properties of Si:P δ -doped layers will ultimately provide a critical theoretical background for experimentalists. Therefore, the focus of this paper is to develop the methodology to handle sufficiently large domains to validate this approach against others, and then to investigate the effect of horizontal and vertical disorder on the electronic structure in highly doped monolayer systems.

Atomistic representation in realistically extended spatial domains is essential to represent dopant disorder effects. The nanoelectronic modeling tool (NEMO3D)^{32–35} can simulate atomistic structures of realistic size and include nonparabolicity of bulk materials automatically by using an empirical $sp^3d^5s^*$ TB model. NEMO3D has been successful in modeling a spectrum of systems in which atomistic details and interface effects are important to understand device behavior, such as phosphorus impurities in silicon devices,^{36–40} valley splitting in miscut Si/SiGe quantum wells,⁴¹ and InGaAs embedded InAs quantum dots.⁴² Having demonstrated our ability to model phosphorus in silicon accurately using an atomistic approach, we expanded NEMO3D's capabilities to run efficiently on peta-scaled computer systems and included a charge-potential self-consistent loop.^{32–35} We now apply NEMO3D-peta to a highly doped Si:P system to explore atomistic effects on the electronic structure of δ -doped layers.

The paper is organized as follows. Section II summarizes the simulation methodology and structure modeling. Section III discusses the electronic structures of Si:P δ -doped layers and shows the effect of disorder on band structures. Section IV summarizes and concludes the paper.

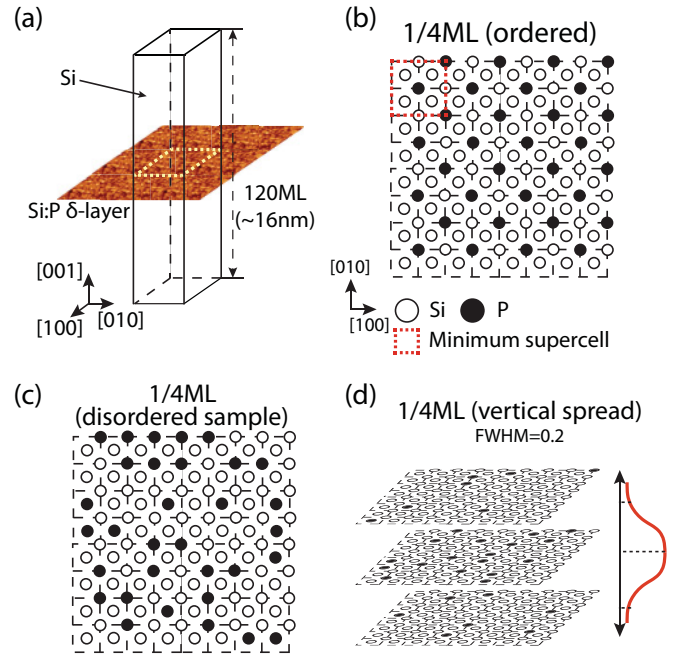


FIG. 1. (Color online) (a) The simulation structure used to represent a 2D Si:P δ -doped layer encapsulated by silicon of thickness 120 ML. 2D periodic boundary conditions are imposed along the doping plane. (b) A perfectly ordered 1/4 ML ($1.7 \times 10^{14} \text{ cm}^{-2}$) Si:P supercell used for the atomistic simulations. In this case, $p(2 \times 2)$ represents the smallest supercell marked in red. (c) An example of a disordered supercell, where $p(8 \times 8)$ is used for disorder simulations. (d) An example representing vertical segregation of the dopants with a Gaussian distribution (FWHM = 0.2 nm). Note: the lattice constant of silicon is $a = 0.357 \text{ nm}$.

II. METHODOLOGY

Simulation structure: The physical structure used in this work is depicted in Fig. 1(a). To represent the infinite sheet of the Si:P δ -layer buried in silicon, periodic boundary conditions are applied to both in-plane directions ([100]/[010]). The silicon substrate and encapsulation layer along [001] is assumed to be intrinsic. We have calculated that at 4 K a minimum confinement thickness of 120 monolayers (ML), or approximately 16 nm is needed to avoid hard wall boundary effects. At such large encapsulation thicknesses we find variations of eigenenergies smaller than 3 meV upon further increase in buffer size. Figure 1(b) shows the top view of δ layer with 1/4 ML ($1.7 \times 10^{14} \text{ cm}^{-2}$) doping density in a *perfectly ordered* $p(8 \times 8)$ unit cell. In such an ordered configuration, the minimum supercell that we can use is $p(2 \times 2)$, which corresponds to 960 atoms with a 120 ML buffer. The $p(8 \times 8)$ cell corresponds to a total atom count of 15,360 atoms. Figure 1(c) shows an example of a disordered dopant configuration. Scrambling the dopant placement can be readily achieved due to the nature of atomistic simulations. However, disorder simulations require a larger supercell of at least $p(8 \times 8)$ to account for random effects in band structures. A similar approach can be applied for electronic structure simulations of III-V or SiGe alloys.⁴³ The vertical straggle of dopants can also be simulated by using Gaussian distributions to model diffusive penetration of dopants from the δ -doped plane

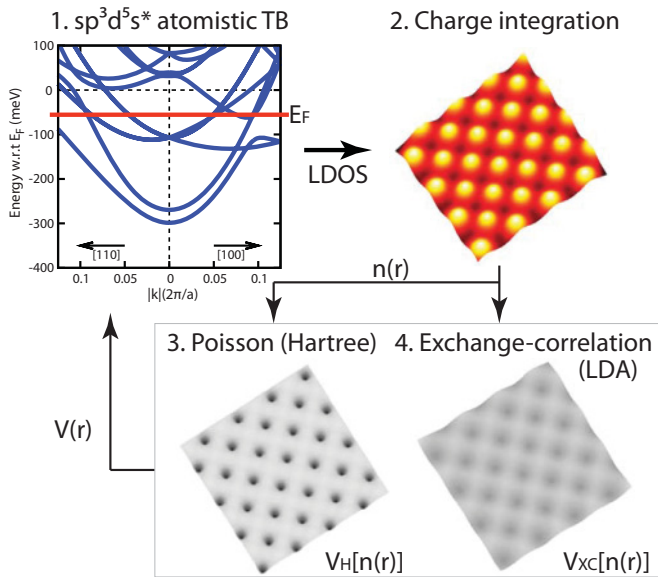


FIG. 2. (Color online) The graphical representation of self-consistent band structure calculation. Eigenstates are computed out of the single electron Schrödinger equation for each k point and subband. The equation is comprised of an atomistic TB Hamiltonian and external potential profiles. The Fermi level (E_F) is determined at the charge neutrality condition which equates the number of electron charge to the number of total impurity charge. The charge is then integrated to determine the electron density $[n(\mathbf{r})]$. The potential profile is subsequently computed at a given electron density. The electrostatic potential $\{V_H[n(\mathbf{r})]\}$ is computed by solving Poisson's equation based on a finite difference grid. A correction is included for electron-electron interaction effects $\{V_{XC}[n(\mathbf{r})]\}$ based on LDA.⁴⁶ The potential profile is the sum of electrostatic and exchange-correlation potentials and it is finally fed back into the Schrödinger solver for the next iteration of the charge calculation.

[Fig. 1(d)]. We use a measurement temperature of 4 K for all numerical experiments. At 4 K it is valid to only consider the conduction band occupation since electrons are only coming from the donor levels and not from thermal excitation from valence bands. Band gap and valence electrons are therefore ignored in the charge calculations presented here, even though our 20 band $sp^3d^5s^*$ model provides accurate results.

Self-consistent procedure: The simulation approach used in this work is to obtain the potential profile and band structure with charge density based self-consistent calculation using NEMO3D-peta.^{44,45} The self-consistent loop has been applied previously to observe the temperature dependence of electronic properties in Si:P δ -doped layers.⁴⁵ The graphical representation of the self-consistent methodology is shown in Fig. 2. First, eigenstates of the δ -doped layer from an atomistic $sp^3d^5s^*$ TB single electron Hamiltonian²⁸ are computed over the first Brillouin zone (BZ) in the discretized 2D k space. Only conduction band states are of interest in these simulations, since the intrinsic carriers are frozen out at low temperature and all carriers in the δ -doped layer are provided by the donors. We can therefore reduce the basis size from 20 to 10 in the $sp^3d^5s^*$ model by only considering a single spin explicitly. This reduces the computational burden by at least a factor of 2. The Fermi level (E_F) of the system is determined iteratively by the charge neutrality condition, which assumes the total number

of electrons to be equal to the number of donors. The local density of states (LDOS) is obtained by binning k states and by integrating the LDOS over the occupied 2D k space, resulting in the electron charge profile $[n(\mathbf{r})]$ of Si:P δ -doped layer.

The electron charge density profile is used to determine two different terms that enter the Schrödinger equation: the Hartree potential and the exchange-correlation potential. The Hartree term $V_H[[n(\mathbf{r})]]$ can be obtained by solving Poisson's equation with a given electron and donor ion profile. All charge contributions are treated as local point charges on a zincblende lattice. Electron-electron interactions must also be taken into account in such many-electron systems. To first order we include an analytical form of exchange and correlation functionals $\{V_{XC}[n(\mathbf{r})]\}$ ⁴⁶ based on the local density approximation (LDA),⁴⁷ which lowers the total energy of the system and modifies the wave function.⁴⁸ To obtain the local charge density in space from the point charge in the atomistic grid, the charge is assumed to be uniform within a finite volume around each atom. The volume around each site is computed as the volume of the unit cell divided by number of atoms per unit cell. Therefore the local electron charge density used for the exchange-correlation potential can be calculated as the amount of charge at each site divided by its surrounding volume. Note that V_{XC} is treated as a linear function of electron density and therefore is computed only for electrons from donors, assuming the exchange-correlation effect of the frozen-out valence electrons $\{V_{XC}[n_V(\mathbf{r})]\}$ of silicon is inherently included in the TB Hamiltonian $\{V_{XC} \approx V_{XC}[n(\mathbf{r})] + V_{XC}[n_V(\mathbf{r})]\}$. More rigorous calculation considering the non-linear behavior of V_{XC} in atomistic TB formalism is beyond the scope of this paper, but can be found in other density-functional based methodologies that also utilizes a TB scheme.⁴⁹

In general, convergence is difficult to achieve because of the sharp potential variations around each impurity location and the low temperature condition. Therefore, the under-relaxed potential $[V(\mathbf{r})]$ is updated for the next iteration of the charge calculation and the charge-potential loop is continued until the mean square value of the potential is converged to within 0.1 meV. Convergence is typically achieved in about 25–35 iteration steps. The computations are carried out on state-of-the-art cluster machines⁵⁰ with 2 GB of memory per core and a typical total compute time of 48 h using 256 cores.

III. RESULTS

A. Equilibrium properties of the ordered Si:P δ layer

Band structure: Figure 3(a) compares the equilibrium band structure of the 1/4 ML Si:P δ -doped layer plotted with respect to the silicon bulk band minimum with the band structure of the pure silicon structure (without the δ -doped layer) of the same minimal unit cell $p(2 \times 2)$ as depicted. The δ -doped layer creates a strong confinement [Fig. 3(b)] and pulls down the bands significantly, causing large splitting between confined subbands. The positions of the 1Γ , 2Γ , Δ valleys, and Fermi level (E_F) all reside under the silicon bulk band edge and are within the confinement potential created by the δ -doped layer. The first few subbands in this band structure can be easily interpreted by the band projection of the bulk silicon valleys as shown in Fig. 4. The two out-of-plane valleys marked in dark

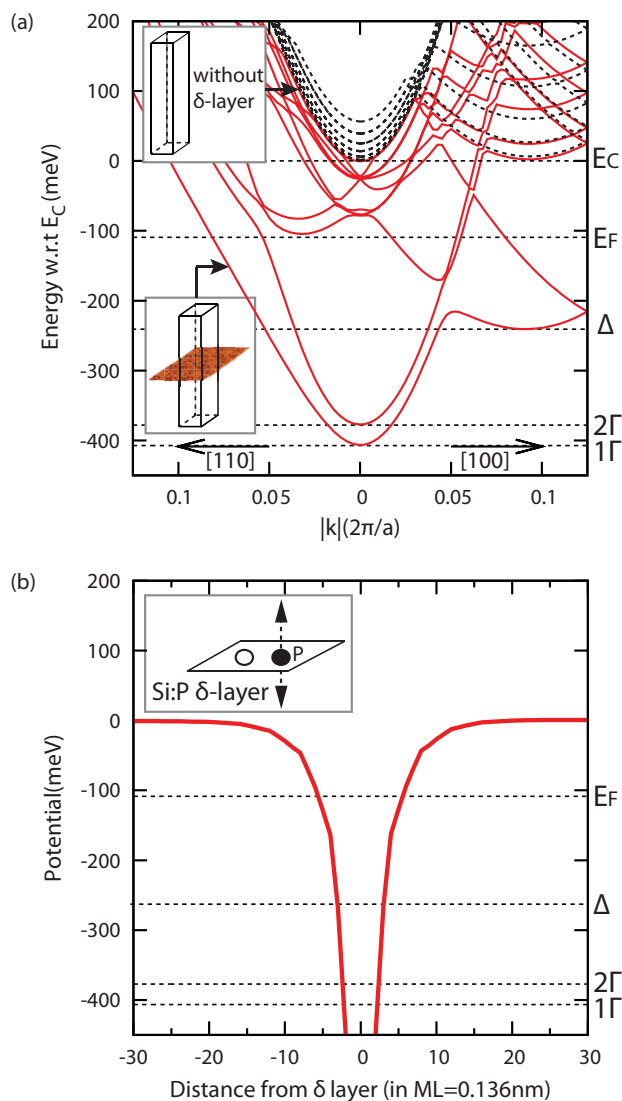


FIG. 3. (Color online) (a) Equilibrium band structure of an ideal ordered 1/4 ML Si:P δ -doped layer at 4 K. The band structure of a pure silicon structure with the same dimension without the δ -doped layer is plotted (dashed line) for comparison. (b) Potential profile plotted along confinement direction ([001]) passing through impurity site. The relative position of the valley minimum point and Fermi level with respect to the silicon conduction band minimum is indicated.

color are projected to the k_x - k_y plane to form 1Γ and 2Γ bands, while the remaining four in-plane valleys are projected along $k_{x,y} = \pm 0.18 \times 2\pi/a$ in the reduced zone scheme. The lower quantization energy ($\propto m^{*-1}$) of Γ -projected valleys is always observed since the confinement mass is larger in Γ -projected valleys ($m_l = 0.91m_0$) than in the remaining in-plane valleys ($m_t = 0.19m_0$). The sharp electrostatic confinement in the z direction due to the screened donor potential creates a very narrow quantum well, which results in a large valley splitting (VS, $E_{2\Gamma} - E_{1\Gamma}$) of ~ 25 meV. This VS in a V-shaped QW⁵¹ is an order of magnitude larger than the VS of typical Si-SiGe quantum wells.⁵²

Table I compares the Fermi level and valley minimum values with results from other methods for the ordered 1/4

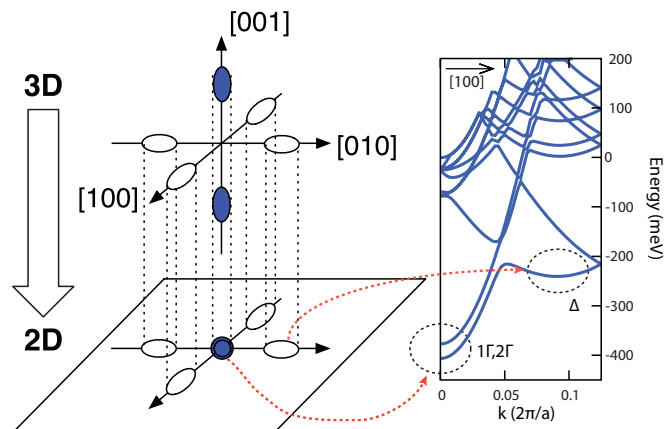


FIG. 4. (Color online) Band projection diagram for the highly confined 2D δ layers. Two valleys (dark) along the z -confinement direction are projected to the Γ point and four other valleys are projected to their own positions.

ML δ -doped layers. The overall comparison results show that the atomistic TB approach predicts reasonable values for the band minima and Fermi level with respect to other methods. Computed Fermi levels stay very close to each other except for the MP method. Since the MP method uses an averaged dopant representation, it may result in a weakly confined potential, which causes a Fermi level shift and reduced valley splitting.³¹ DFT predicts a larger VS and lower Γ valleys but a higher Δ valley. PP shows similar values to our results but smaller VS. A major difference of the PP method can be seen by comparing the details of the band structure, which for PP is based on a parabolic band assumption.²⁵ Details such as nonparabolicity and band anticrossing, which may cause nonlinear modulation of low-bias conductance, are not taken into account in the PP method.

Potential and charge: The charge profile along the confinement or z direction is shown in Fig. 5. 96% of the charge is confined vertically within 21 monolayers (< 3 nm) from the donor positions, leaving the donor charges in the δ -doped layer perfectly screened. Therefore, the potential profile along the confinement direction decays faster than the ideal Coulombic potential ($\propto r^{-1}$) and the local field vanishes within a range of ± 20 monolayers (± 3 nm) from the δ -doped layer. Our charge distribution (FWHM = 0.81 nm = 7 ML) agrees well with both DFT and MP calculations, which predict 0.67 nm (DFT) and 0.84 nm (MP), respectively.^{30,31} The temperature dependence of the charge screening in such Si:P δ -doped layers is described further in Ref. 45.

TABLE I. Energies obtained from different models of the 1/4 ML Si:P 2D δ layers showing the Fermi energy, 1Γ , 2Γ , and 1Δ bands in meV (reference: silicon $E_C = 0.0$ meV).

Approach	E_F	1Γ	2Γ	1Δ
This work	-110	-394	-369	-242
Wannier/PP ²⁵	-111	-410	-400	-270
TB (sp^3s^*) ²⁶	-110	N/A	N/A	N/A
DFT ³⁰	-110	-540	-420	-210
DFT/MP ³¹	-62	-445	-425	-236

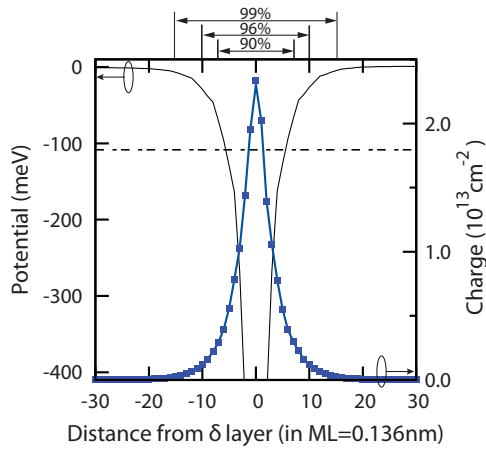


FIG. 5. (Color online) Charge profile of a perfectly ordered 1/4 ML Si:P δ -doped layer at 4 K. 90%, 96%, and 99% of the charge is confined within 15 (2.03 nm), 21 (2.85 nm), and 31 (4.21 nm) ML, respectively. For reference, FWHM = 7 ML (0.81 nm) and it contains 66% of the charge.

B. The effect of doping density in the Si:P δ layer

To examine the doping density dependence on the Si:P δ -doped layer band structure, different numbers of impurities are placed in a $4a \times 4a$ simulation domain. The doping density conversion table which relates the discrete atomistic density with the more common per square centimeter density is provided in Table II. As the doping density increases, more subbands are occupied under the Fermi level to maintain charge neutrality. Stronger electrostatic coupling contributes to a further downshift of the subbands, promoting an increased number of occupied subbands [Fig. 6(a)]. Our model predicts a linear dependence of the critical 1Γ , 2Γ , and Δ energies as a function of doping density as shown in Fig. 6(b). A slight increase in VS as the doping density increase indicates that the potential confinement of the δ -doped layer is also becoming stronger. A more gradual trend of the Δ valley compared to Γ valleys is predicted since the density of states (DOS) effective mass of the Δ valley is larger. In other words, even a small inclusion of sub-bands originating from Δ valleys causes a

TABLE II. Conversion table between doping constant and number of impurities in the $4a \times 4a$ supercell. Total number of atoms in the δ layer is 32.

P coverage	1/6.4	1/5.3	1/4.6	1/4.0	1/3.6	1/3.2	1/2.9
Doping (10^{14} cm^{-2})	1.06	1.27	1.48	1.70	1.91	2.12	2.33
Impurities	5	6	7	8	9	10	11

larger increase in DOS and occupied states compared to the lighter Γ valley subbands.

C. The effect of disorder in the Si:P δ layer

In reality it is impossible to make a perfectly arranged infinite δ -doped layer. Random dopant incorporation causes a disordered donor configuration within the Si:P δ -doped layer. The Si:P system can be viewed as a *random alloy* system with a different set of bonding parameters (Si-P, P-Si, Si-Si) and an additional electrostatic potential caused by the donor charges screened by their electrons. This is analogous to typical III-V and Si-Ge alloys in heterostructures that have different TB and strain parameters and bond lengths. For δ -doped layers, however, it is computationally more intensive to obtain the dispersion since the potential has to be computed self-consistently. The simulation of such random alloy systems is generally performed with repeated supercells that represent the randomness. While true band structures only exist for large supercells, the existence of band gaps and effective masses in alloys validates the concept of an approximate band structure.⁵³

Supercell geometry: To represent the electronic properties of a realistic alloy system, a large enough supercell is needed to mimic the random nature of the target system and to consider a sufficient number of statistical samples. Since the potential profile in a Si:P δ -doped layer requires heavy computation, it is difficult to collect enough samples without a reduced supercell. Therefore, to set up a reasonable supercell geometry, the size is first increased to $8a \times 8a$ in the periodic plane to appropriately represent randomness (Fig. 1). The cladding thickness is reduced to save the overall computational burden

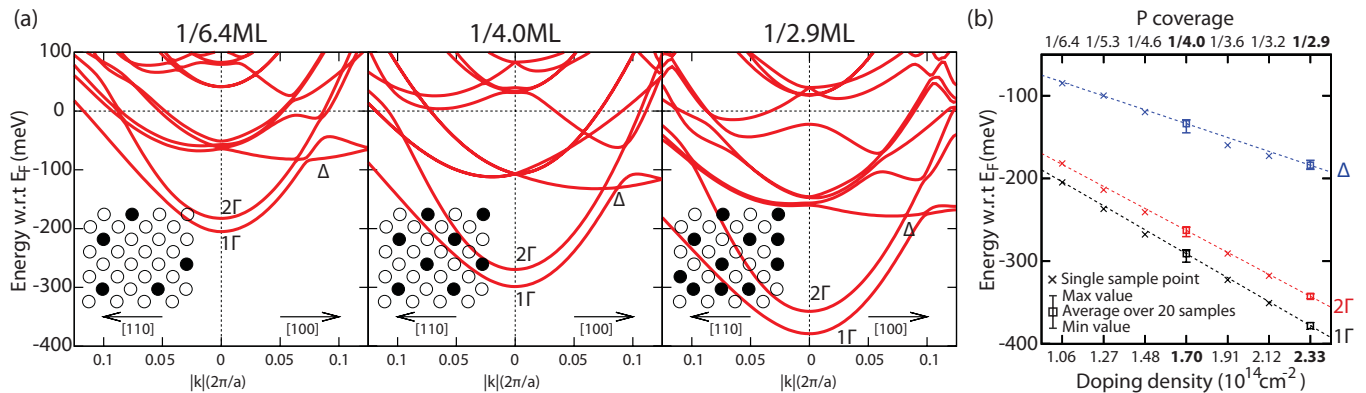


FIG. 6. (Color online) (a) Band structure results of 1/6.4, 1/4.0, and 1/2.9 ML δ -doped layers. Inset in each band structure plot provides dopant placement used for the simulation. Due to odd number of dopants in 1/6.4 and 1/2.9 ML cases, unavoidable disorders are present. (b) Valley minimum values of different doping densities plotted with respect to the Fermi level. Statistical samples of 1/4.0 and 1/2.9 ML cases are plotted against other doping cases.

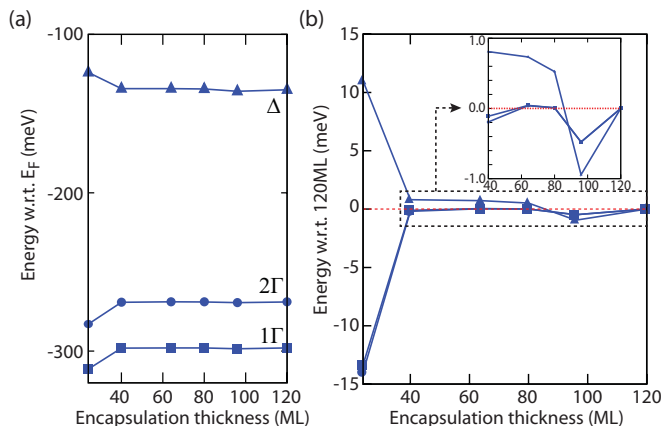


FIG. 7. (Color online) (a) Eigenvalues of valley minima with respect to Fermi levels vs encapsulation thickness. The relative position stays constant down to 64 ML regardless of the thickness. (b) Energy change of 1Γ , 2Γ , and Δ measured against 120 ML structure. Inset provides a zoom-in view of energy difference down to 40 ML and difference is less than 1 meV.

and to enable the collection of a sufficient number of samples. To determine the minimum cladding thickness to satisfy the above conditions without losing any physical meaning due to artificial domain boundaries, the valley minima with respect to the corresponding Fermi levels are compared with varying encapsulation thicknesses (120, 96, 80, 64, 40, and 24 ML). As shown in Fig. 7, valley energies vary little within 1 meV indicating the minimal effect on the band structure down to 40 ML. Therefore it is reasonable to reduce the encapsulation thickness from 120 to 64 ML in modeling disordered samples, which reduces the overall computational burden by 50%.

In-plane disorder: Initially, we considered a δ -doped layer with a disordered dopant configuration within the atomic dopant plane. Figure 8 compares the effect of disorder with a $1/4$ ML ordered supercell. Multiple band crossings of the Γ and Δ originating bands occur due to the repeating supercell structure as shown in Fig. 8(a). In contrast, disordered configurations couple some of these bands such that they anticross. The disordered dopant configuration used for the disordered sample [Fig. 8(a)] also breaks the translational symmetry along $[100]/[010]$, introducing distortions to every subband. AC1–AC2 and AC3–AC4 labeled in the band structures in Fig. 8(a) are the major anticrossings in the impurity subbands for the ordered and disordered cases, respectively. Figures 8(b) and 8(c) compare the effects of disorder on the potential and charge density in the impurity plane. The disordered charge shows a significant charge accumulation in impurity clusters, while the ordered array shows a much smoother background charge distribution. However, the randomness causes little change in the positions of the 1Γ , 2Γ , and Δ valleys, as seen in Fig. 6(b) where the statistical results of valley energies for $1/2.9$ and $1/4.0$ ML are indicated.

Since the band structure of the large supercell is complicated without much insight beyond the lowest two band edges, we also study the density of states (DOS). Figure 9 compares the DOS between the ordered and disordered Si:P δ -doped layers. The ordered layer (Fig. 9, dashed line), shows a nonparabolicity of the first two subbands as seen from the

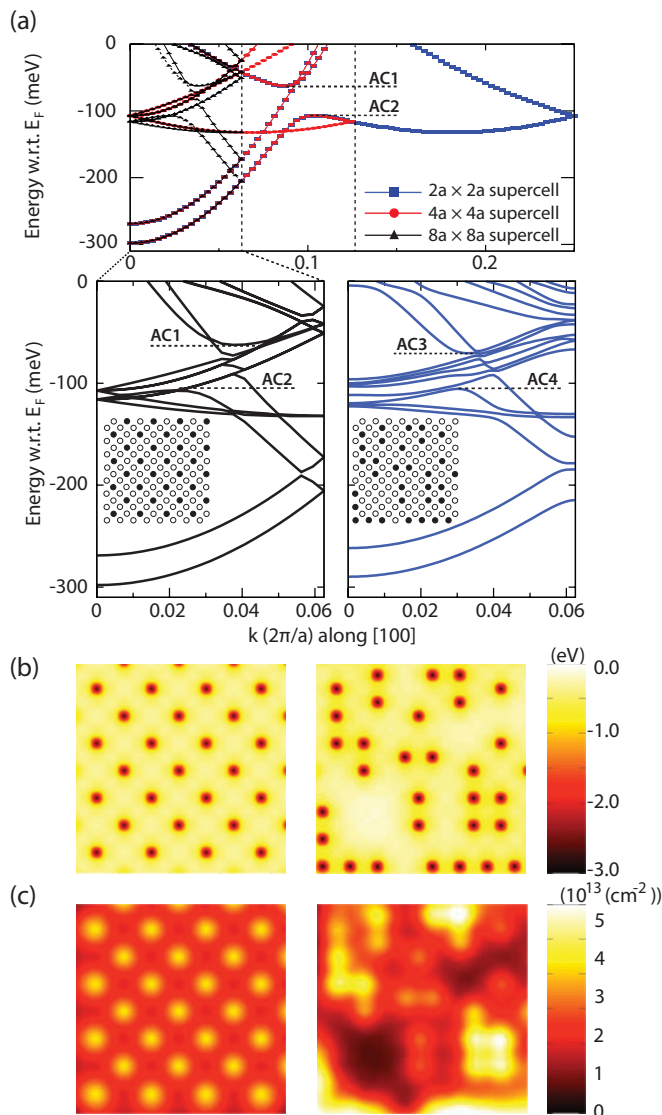


FIG. 8. (Color online) (a) Band structure comparison between ordered and an example of disordered supercell. Zone unfolding relationship in the perfectly ordered case is displayed (top) and the band structure of ordered $8a \times 8a$ supercell (bottom left) is shown next to the disordered supercell (bottom right) for direct comparison. AC1–AC2 and AC3–AC4 indicate gaps due to the band anticrossing in the ordered and disordered supercell, respectively. The anticrossings affect the density of states distribution, which will be discussed in Fig. 9. Comparison of the (b) potential and (c) charge profile between ordered and in-plane disordered supercell shown in (a).

gradual increase in the DOS. A perfectly parabolic dispersion would show a flat DOS. The steep increase in the DOS at -130 meV indicates the turn-on of the Δ bands, which have a larger DOS mass ($m_l = 0.9 > m_l = 0.19$). The first subband (1Γ) turns off at around -100 meV due to band anticrossing, resulting in a decrease of the DOS at this energy as observed. At the AC1–AC2 gap in Fig. 9, the DOS is lowered due to anticrossing of the impurity bands indicated in Fig. 8(a).

The DOS for the disordered δ -doped layer (red line) has a couple of interesting features compared to the ordered case. The disordered DOS in Fig. 9 is averaged over 20

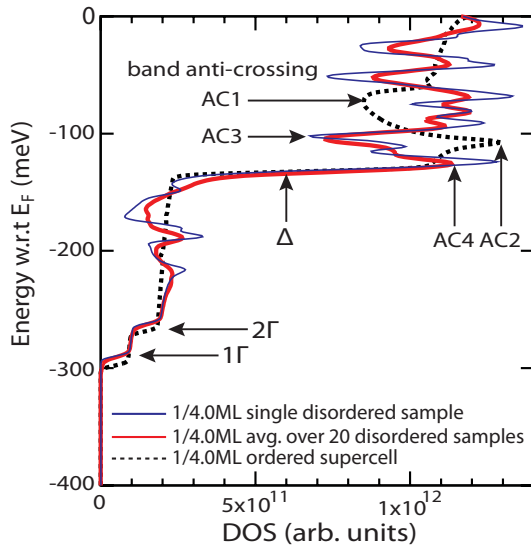


FIG. 9. (Color online) DOS comparison between ordered (dashed line) and disordered Si:P δ -doped layers (solid lines). Fluctuations in DOS for ordered supercell is shown between AC1 and AC2 which is caused by band anticrossing labeled in Fig. 8(a). Similar fluctuation is also captured in disordered supercell between AC3 and AC4. For disordered cases, the DOS for single sample (blue) and the DOS averaged over 20 samples (red) are indicated.

statistical samples. Again, the Δ valley contribution can be identified easily regardless of complicated subband splitting. This subband splitting in addition to the gaps in the BZ boundaries create additional fluctuations in the DOS as indicated in the energy range AC3–AC4 of Figs. 8(a) and 9. Despite these additional DOS fluctuations, the overall DOS appears very similar to the ideally ordered DOS and the DOS is large enough to constantly provide electrons to the attached narrow leads, which clearly have a smaller DOS. We note that it is the DOS fluctuation at the Fermi level that will modulate the conductance in the low bias regime. However, the variation of the conductance is expected to be minimal among samples fabricated under the same doping density.

Out-of-plane (vertical) disorder: Finally, to simulate what would happen if there were dopant diffusion leading to disorder out of the δ -doped layer, a Gaussian distribution of dopants with a varying FWHM is considered assuming a vertical segregation of no more than 7 layers, or 0.81 nm. To date the maximum limit of vertical segregation of δ -doped layers encapsulated at low temperatures of 250 °C has been measured experimentally to be 0.58 nm.¹¹ To mimic this finding in simulation, 1/4 ML is taken into account and an ensemble of 20 samples for every case (FWHM = 0.0, 0.15, 0.2, 0.3, and 0.4 nm) is considered.

Figure 10(a) compares the valley minimum values of these samples. Spreading out the doping out of the central layer can be associated with a weak doping reduction in that particular layer. Such doping reduction allows the impurity bands to rise slightly in energy (compare with Fig. 6). A more significant effect is seen by the reduction of the strong confinement, which will be most evident in the VS between the Γ valleys [Fig 10(b)]. A perfect Si:P δ -doped layer exhibits large VS (~ 27 meV) with small variations. On the

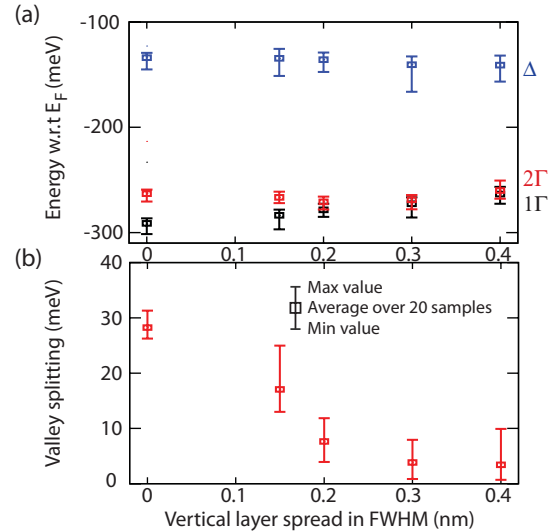


FIG. 10. (Color online) (a) 1Γ , 2Γ , and Δ valley minimum values are plotted with respect to the Fermi level vs vertical impurity segregation. Statistical samples of vertical segregation of dopant atoms with a nominal 1/4 ML doping is considered. (b) Valley splitting as a function of vertical segregation.

contrary, as the vertical impurity segregation increases, the VS decreases significantly. As a result measuring the VS experimentally, such as by using Schottky-barrier tunneling spectroscopy,^{18,20,54,55} can be used to determine the degree of vertical dopant diffusion.

IV. CONCLUSION

We use an empirical tight binding, self-consistent potential approach to model realistically extended Si:P δ -doped layer structures. The methodology is validated against other approaches, such as DFT and pseudopotential methods. The scalability of the NEMO methodology enables us to study supercells that resemble realistically disordered systems. We compare statistical samples for dopant disorder in the doping plane and out of the doping plane, and study the sensitivity to doping density. The δ -doped layer creates a Coulombic quantum well that confines electrons in a dense quasimetallic impurity band under the standard silicon conduction band. An increased doping density is found to increase the confinement and to lower the impurity band energies. The 1Γ , 2Γ , and Δ bands all depend linearly on the doping, but react to doping changes at a different rate, mainly due to the DOS effective mass difference. In-plane disorder is predicted to only weakly affect the VS and DOS of the quasimetallic sheet. Doping disorder leads to an increased DOS modulation close to the Fermi energy, thus in turn leading to stronger conductance variation with device gating. Out-of-plane disorder shows a significant effect on the band edges and VS. VS is predicted to be reduced with increased out-of-plane disorder. The strong VS modulation may serve as a metrology tool to gauge vertical doping straggle in a well-controlled sequence of experiments. With extensive simulation results, we provide new information about the properties of these highly confined sheets that will guide experimentalists in understanding and validating electronic properties of Si:P δ -doped layers.

ACKNOWLEDGMENTS

NSF-funded nanoHUB.org and TeraGrid resources provided by the National Institute for Computational Sciences (NICS) and the Texas Advanced Computing Center (TACC) computational resources were used in this work. This research was conducted by the Australian Research Council Centre

of Excellence for Quantum Computation and Communication Technology (Project No. CE110001027). The research was also supported by the US National Security Agency and the US Army Research Office under Contract No. W911NF-08-1-0527. The authors would like to thank the reviewers for insightful comments. The authors also acknowledge Yui-Hong Tan for spending his time on improving this manuscript.

*sunnyleekr@purdue.edu

†http://nanohub.org

‡http://www.cqc2t.org

¹M. Y. Simmons, S. R. Schofield, J. L. O'Brien, N. J. Curson, L. Oberbeck, T. Hallam, and R. G. Clark, *Surf. Sci.* **532-535**, 1209 (2003).

²F. J. Rueß, L. Oberbeck, M. Y. Simmons, K. E. J. Goh, A. R. Hamilton, T. Hallam, S. R. Schofield, N. J. Curson, and R. G. Clark, *Nano Lett.* **4**, 1969 (2004).

³F. J. Rueß, W. Pok, K. E. J. Goh, A. R. Hamilton, and M. Y. Simmons, *Phys. Rev. B* **75**, 121303 (2007).

⁴M. Fuechsle, S. Mahapatra, F. A. Zwanenburg, M. Friesen, M. A. Eriksson, and M. Y. Simmons, *Nat. Nanotechnol.* **5**, 502 (2010).

⁵F. J. Rueß, B. Weber, K. E. J. Goh, O. Klochan, A. R. Hamilton, and M. Y. Simmons, *Phys. Rev. B* **76**, 085403 (2007).

⁶B. Kane, *Nature (London)* **393**, 133 (1998).

⁷R. Vrijen, E. Yablonovitch, K. Wang, H. W. Jiang, A. Balandin, V. Roychowdhury, T. Mor, and D. DiVincenzo, *Phys. Rev. A* **62**, 012306 (2000).

⁸L. C. L. Hollenberg, A. S. Dzurak, C. Wellard, A. R. Hamilton, D. J. Reilly, G. J. Milburn, and R. G. Clark, *Phys. Rev. B* **69**, 113301 (2004).

⁹C. D. Hill, L. C. L. Hollenberg, A. G. Fowler, C. J. Wellard, A. D. Greentree, and H. S. Goan, *Phys. Rev. B* **72**, 045350 (2005).

¹⁰L. C. L. Hollenberg, A. D. Greentree, A. G. Fowler, and C. J. Wellard, *Phys. Rev. B* **74**, 045311 (2006).

¹¹L. Oberbeck, N. J. Curson, M. Y. Simmons, R. Brenner, A. R. Hamilton, S. R. Schofield, and R. G. Clark, *Appl. Phys. Lett.* **81**, 3197 (2002).

¹²K. E. J. Goh, L. Oberbeck, M. Y. Simmons, A. R. Hamilton, and R. G. Clark, *Appl. Phys. Lett.* **85**, 4953 (2004).

¹³K. E. J. Goh, Y. Augarten, L. Oberbeck, and M. Y. Simmons, *Appl. Phys. Lett.* **93**, 142105 (2008).

¹⁴K. E. J. Goh and M. Y. Simmons, *Appl. Phys. Lett.* **95**, 142104 (2009).

¹⁵H. F. Wilson, O. Warschkow, N. A. Marks, S. R. Schofield, N. J. Curson, P. V. Smith, M. W. Radny, D. R. McKenzie, and M. Y. Simmons, *Phys. Rev. Lett.* **93**, 226102 (2004).

¹⁶H. F. Wilson, O. Warschkow, N. A. Marks, N. J. Curson, S. R. Schofield, T. C. G. Reusch, M. W. Radny, P. V. Smith, D. R. McKenzie, and M. Y. Simmons, *Phys. Rev. B* **74**, 195310 (2006).

¹⁷S. R. Schofield, N. J. Curson, M. Y. Simmons, F. J. Rueß, T. Hallam, L. Oberbeck, and R. G. Clark, *Phys. Rev. Lett.* **91**, 136104 (2003).

¹⁸G. Tempel, F. Koch, H. P. Zeindl, and I. Eisele, *J. Phys. Colloq.* **48**, C5-259 (1987).

¹⁹I. Eisele, *Appl. Surf. Sci.* **36**, 39 (1989).

²⁰I. Eisele, *Superlattices Microstruct.* **6**, 123 (1989).

²¹L. M. Gaggero-Sager, M. E. Mora-Ramos, and D. A. Contreras-Solorio, *Phys. Rev. B* **57**, 6286 (1998).

²²L. Gaggero-Sager, S. Vlaev, and G. Monsivais, *Comput. Mater. Sci.* **20**, 177 (2001).

²³A. L. Rosa, L. M. R. Scolfaro, R. Enderlein, G. M. Sipahi, and J. R. Leite, *Phys. Rev. B* **58**, 15675 (1998).

²⁴L. M. R. Scolfaro, D. Beliaev, R. Enderlein, and J. R. Leite, *Phys. Rev. B* **50**, 8699 (1994).

²⁵G. Qian, Y. C. Chang, and J. R. Tucker, *Phys. Rev. B* **71**, 045309 (2005).

²⁶X. Cartoixa and Y. C. Chang, *Phys. Rev. B* **72**, 125330 (2005).

²⁷G. Klimeck, R. C. Bowen, T. B. Boykin, C. Salazar-Lazaro, T. A. Cwik, and A. Stoica, *Superlattices Microstruct.* **27**, 77 (2000).

²⁸J. M. Jancu, R. Scholz, F. Beltram, and F. Bassani, *Phys. Rev. B* **57**, 6493 (1998).

²⁹T. B. Boykin, G. Klimeck, and F. Oyafuso, *Phys. Rev. B* **69**, 115201 (2004).

³⁰D. J. Carter, O. Warschkow, N. A. Marks, and D. R. McKenzie, *Phys. Rev. B* **79**, 033204 (2009).

³¹D. J. Carter, N. A. Marks, O. Warschkow, and D. R. McKenzie, *Nanotechnology* **22**, 065701 (2011).

³²G. Klimeck, F. Oyafuso, T. B. Boykin, R. C. Bowen, and P. von Allmen, *Comput. Model. Eng. Sci.* **3**, 601 (2002).

³³G. Klimeck, S. Ahmed, H. Bae, N. Kharche, S. Clark, B. Haley, S. Lee, M. Naumov, H. Ryu, F. Saied, M. Prada, M. Korkusinski, T. Boykin, and R. Rahman, *IEEE Trans. Electron Devices* **54**, 2079 (2007).

³⁴G. Klimeck, S. Ahmed, N. Kharche, M. Korkusinski, M. Usman, M. Prada, and T. Boykin, *IEEE Trans. Electron Devices* **54**, 2090 (2007).

³⁵S. Ahmed, N. Kharche, R. Rahman, M. Usman, S. Lee, H. Ryu, H. Bae, S. Clark, B. Haley, M. Naumov, F. Saied, M. Korkusinski, R. Kennel, M. McLennan, T. B. Boykin, and G. Klimeck, *Encyclopedia of Complexity and Systems Science* (Springer, New York, 2009), pp. 5745–5783.

³⁶G. P. Lansbergen, R. Rahman, C. J. Wellard, I. Woo, J. Caro, N. Collaert, S. Biesemans, G. Klimeck, L. C. L. Hollenberg, and S. Rogge, *Nat. Phys.* **4**, 656 (2008).

³⁷R. Rahman, C. J. Wellard, F. R. Bradbury, M. Prada, J. H. Cole, G. Klimeck, and L. C. L. Hollenberg, *Phys. Rev. Lett.* **99**, 036403 (2007).

³⁸R. Rahman, S. H. Park, J. H. Cole, A. D. Greentree, R. P. Muller, G. Klimeck, and L. C. L. Hollenberg, *Phys. Rev. B* **80**, 035302 (2009).

³⁹R. Rahman, S. H. Park, T. B. Boykin, G. Klimeck, S. Rogge, and L. C. L. Hollenberg, *Phys. Rev. B* **80**, 155301 (2009).

⁴⁰R. Rahman, G. P. Lansbergen, S. H. Park, J. Verduijn, G. Klimeck, S. Rogge, and L. C. L. Hollenberg, *Phys. Rev. B* **80**, 165314 (2009).

- ⁴¹N. Kharche, M. Prada, T. B. Boykin, and G. Klimeck, *Appl. Phys. Lett.* **90**, 092109 (2007).
- ⁴²M. Usman, H. Ryu, I. Woo, D. Ebert, and G. Klimeck, *IEEE Trans. Nanotech.* **8**, 330 (2009).
- ⁴³N. Kharche, M. Luisier, T. Boykin, and G. Klimeck, *J. Comput. Elec.* **7**, 350 (2008).
- ⁴⁴S. Lee, H. Ryu, Z. Jiang, and G. Klimeck, in *13th International Workshop on Computational Electronics 2009, IWCE'09* (Beijing, 2009).
- ⁴⁵H. Ryu, S. Lee, and G. Klimeck, in *13th International Workshop on Computational Electronics 2009, IWCE'09* (Beijing, 2009).
- ⁴⁶E. Gawlinski, T. Dzurak, and R. A. Tahir-Kheli, *J. Appl. Phys.* **72**, 3562 (1992).
- ⁴⁷R. G. Parr and W. Yang, *Density-functional Theory of Atoms and Molecules* (Oxford University Press, 1994).
- ⁴⁸E. Wigner, *Phys. Rev.* **46**, 1002 (1934).
- ⁴⁹T. Frauenheim, G. Seifert, M. Elstner, Z. Hajnal, G. Jungnickel, D. Porezag, S. Suhai, and R. Scholz, in *Computer Simulation of Materials at Atomic Level* (Wiley, New York, 2005), pp. 41–62.
- ⁵⁰[<http://top500.org>].
- ⁵¹T. B. Boykin, G. Klimeck, P. von Allmen, S. Lee, and F. Oyafuso, *J. Appl. Phys.* **97**, 113702 (2005).
- ⁵²T. B. Boykin, G. Klimeck, M. A. Eriksson, M. Friesen, S. N. Coppersmith, P. von Allmen, F. Oyafuso, and S. Lee, *Appl. Phys. Lett.* **84**, 115 (2004).
- ⁵³T. B. Boykin, N. Kharche, G. Klimeck, and M. Korkusinski, *J. Phys. Condens. Matter* **19**, 036203 (2007).
- ⁵⁴D. C. Tsui, *Phys. Rev. Lett.* **24**, 303 (1970).
- ⁵⁵M. Zachau, F. Koch, K. Ploog, P. Roentgen, and H. Beneking, *Solid State Commun.* **59**, 591 (1986).